High Power Laser Science and Engineering, (2024), Vol. 12, e13, 15 pages.
doi:10.1017/hpl.2023.88

HIGH POWER LASER SCIENCE AND ENGINEERING

RESEARCH ARTICLE

Mismatch analysis of all-fiber coherent beam combiners based on the self-imaging effect

Yuefang Yan[1,2], Yu Liu[1], Haoyu Zhang[1], Yuwei Li[1], Chao Guo[1], Qiang Shu[1], Wenhui Huang[2], Feng Jing[1], and Rumao Tao[1]

[1] *Laser Fusion Research Center, China Academy of Engineering Physics, Mianyang, China*

[2] *Key Laboratory of Particle & Radiation Imaging (Tsinghua University), Ministry of Education, Beijing, China*

(Received 9 April 2023; revised 16 October 2023; accepted 10 November 2023)

Abstract

All-fiber coherent beam combiners based on the self-imaging effect can achieve a near-perfect single laser beam, which can provide a promising way to overcome the power limitation of a single-fiber laser. One of the key points is combining efficiency, which is determined by various mismatches during fabrication. A theoretical model has been built, and the mismatch error is analyzed numerically for the first time. The mismatch errors have been numerically studied with the beam quality and combining efficiency being chosen as the evaluation criteria. The tolerance of each mismatch error for causing 1% loss is calculated to guide the design of the beam combiners. The simulation results are consistent with the experimental results, which show that the mismatch error of the square-core fiber is the main cause of the efficiency loss. The results can provide useful guidance for the fabrication of all-fiber coherent beam combiners.

Keywords: all-fiber; coherent beam combination; mismatch analysis; self-imaging

1. Introduction

High-power fiber lasers with near-diffraction-limited beam quality have become powerful and versatile laser sources, which are widely used in many application scenarios[1–6]. To deepen the present applications and open up new avenues, higher laser powers are required, and power scaling is the one of the persistent goals of global researchers. The laser power from a single fiber with the few-mode guiding property is limited by various physical effects and engineering realizability, including the nonlinear effects, mode instability, available pump power, and so on[7–9]. The maximal power of a near-diffraction-limited laser from a single fiber has been halted around 20 kW for nearly 10 years[10,11], which is far below the power thresholds in some advanced application scenarios. In order to break the aforementioned limitations, scientists have proposed various beam combination technologies, using which a beyond-limited high-power laser could be realized by combining multiple medium-power fiber lasers[12–14]. Among these beam combining methods, coherent beam combination (CBC) can scale up the optical power while maintaining the laser beam quality, which means that it can achieve an enhancement of the brightness of the laser. CBC has attracted extensive attention and experienced rapid development in recent years, and more than 10 kW single-mode lasers have already been demonstrated[15–17]. However, CBC with multi-kilowatt-level operation has almost been achieved with a free-space configuration, and a number of free-space optical elements and the control units thereof have to be employed[16,18–21], which results in systems that are bulky and complex.

As is well known, the all-fiber scheme, on the other hand, has the advantages of a compact structure, being free of alignment and having a long-term stable performance. The design and fabrication of high-power all-fiber components also has boosted the rapid development and wide application of fiber lasers[22–24]. Therefore, CBC using an all-fiber combiner can bypass the issues brought about by traditional free-space structures[25–28], and is promising from the laser engineering aspect. In Ref. [29], our group proposed an all-fiber CBC method based on the self-imaging effect, which has the potential to obtain a single laser beam with nearly 100% efficiency. Then, a 2 × 2 all-fiber coherent beam combiner was experimentally demonstrated, but the efficiency was only about 52.7%[30,31]. The discrepancy between the theoretical prediction and the experimental result is mainly attributed to the deviation from the optimal combiner design, which is a key factor for improving the CBC performance, but there is a lack of thorough investigations so far.

Correspondence to: Rumao Tao, Laser Fusion Research Center, China Academy of Engineering Physics, Mianyang 621900, China. Email: supertaozhi@163.com

In this paper, theoretical modeling of the all-fiber coherent beam combiner based on the self-imaging effect is carried out, and three types of mismatch errors are characterized and analyzed using the finite difference beam propagation method (FDBPM)[32,33]. Both the beam quality (M^2) and combining efficiency are calculated to evaluate the beam combining performance. Moreover, the tolerance of each mismatch error for causing 1% loss is given, and some instructive discussions are also presented. Finally, the experimental results are analyzed by the theoretical model, which reveals the main factors of the combining loss and provides improvement directions for the design and fabrication of the coherent beam combiner.

2. Categories of mismatch during all-fiber coherent beam combiner fabrication

The all-fiber coherent beam combiner based on the self-imaging effect is composed of three parts: an input fiber array, a square-core fiber and an end-cap, as Figure 1 shows. The input fiber array is a plurality of polarization-maintaining large-mode-area (PLMA) passive fibers arranged in a square pattern, generally with the help of a capillary tube to confine the shape. The square-core fiber has a specific length at which the self-imaging effect of the laser can be enabled[34]. The end-cap is employed to reduce the laser intensity at the glass–air interface so as to allow high-power operation. In principle, high-efficiency and high-beam-quality CBC based on the self-imaging effect requires that the individual lasers should be aligned perfectly with respect to the self-imaging waveguide, and the self-imaging waveguide must have the ideal square shape. Phase control is also essential but is outside the scope of this paper. In order to guarantee that the fiber array injects lasers into the square-core fiber at the right position, the input fibers need to be tapered down to a certain size, which is matched with the core dimension of the square-core fiber, and the side-length direction should be aligned to that of the square-core fiber by viewing the cross-sectional images. Nevertheless, imperfections of the fabrication process of the fiber combiner are inevitable, which lead to mismatch errors and result in a deterioration of the combining efficiency and beam quality. Moreover, the square-core fiber also exhibits discrepancy in the geometry from the theoretical self-imaging waveguide, which further worsens the combining performance. Therefore, in order to give indications for the design and fabrication of square-core fiber and the fiber combiner, three types of mismatch errors are analyzed in this paper: the alignment error of the fiber array, the assembly error between the fiber array and the square-core fiber and the geometric error of the square-core fiber, which are described in detail in the following.

2.1. Alignment error of the fiber array

In order to deliver a high-power laser with linear polarization, PLMA fibers are used to construct the square-distributed fiber array with the assistance of a glass tube, as shown in Figure 2. Due to many practical factors, for

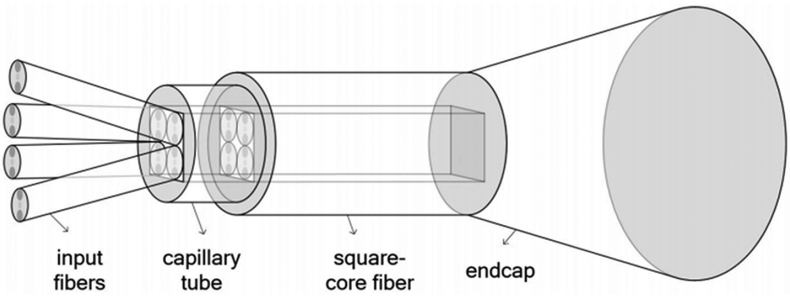

Figure 1. Diagram of the all-fiber coherent beam combiner based on the self-imaging effect.

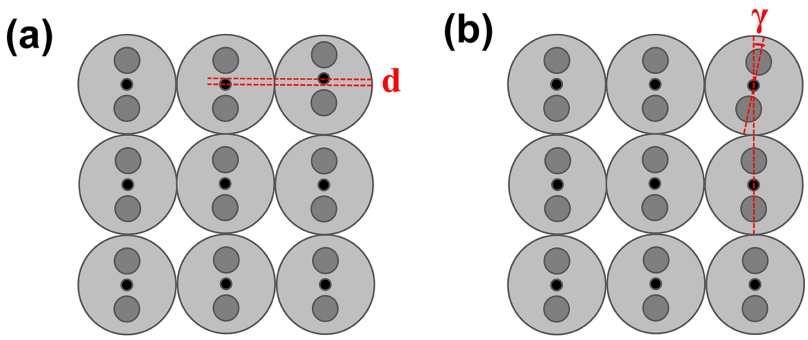

Figure 2. Diagram of (a) the position error and (b) the polarization deviation of the fiber array.

instance, the size difference of the bundled fibers, the eccentricity of the core of individual fibers, the geometrical error of the confining tube, the rolling of fibers caused by instable geometrical distribution and so on, position errors of the fiber cores are introduced. As sketched in Figure 2(a), a parameter d is used to denote the distance deviation of fiber cores from the ideal self-imaging position. Apart from the requirement of the laser injection position, that is, the fiber core position, the ideal CBC also needs the lasers to have the same polarization, but due to alignment precision issues, it is difficult to obtain perfect consistency of the polarization directions of the bundled fibers, which also deteriorates the combining performance. A diagram of the polarization deviation is shown in Figure 2(b). The parameter γ is used to represent the angular difference between the actual polarization direction and the designed direction, which is assumed to be along the y-axis. The clockwise deviation is positive and the counterclockwise deviation is negative.

2.2. Assembly error between the fiber array and the square-core fiber

The fiber array and the square-core fiber are assembled through a fiber fusion process, during which a position error and a pointing error may occur, as Figure 3 shows. The position error is mainly generated from the alignment mismatch between the fiber array and the square-core fiber, and can be divided into two categories: one is the transversal offset D induced by the imprecision of side-view alignment or the eccentricity of the square-core fiber, while the other is the angular offset ε in the cross-sectional plane, which is mainly due to the imprecision of end-view alignment. The pointing error α, on the other hand, is caused by the cleave angle of the fiber array or of the square-core fiber. All the mismatch factors will contribute to the combining loss and beam-quality degradation.

2.3. Geometric error of the square-core fiber

As for the square-core fiber, suffering from the effect of surface tension during the fiber drawing process, the cross-sectional geometry of fiber core will become more rounded compared to the original preform and, thus, it is difficult for the core to maintain the ideal square shape, as Figure 4(a) shows. The deviation contains two parts: firstly, the four corners of the core are not right angles but rather rounded at a curvature radius denoted by r; secondly, the four sides of the core are not straight but rather curved inwards or outwards, and the deviation that occurs at the mid-point of the side is denoted by h. In order to simplify the calculations, it is assumed that the radii of the four rounded corners are the same and the deviations of the four rounded sides are also identical. Moreover, being affected by the shaping error of the fiber preform, for instance, one side is not perpendicular to the adjacent sides but with an angle θ, as shown in Figure 4(b), the square-core fiber will inherit the geometrical error, which affects the self-imaging performance. Besides, the square-core fiber also has other geometrical issues. The fiber core may be twisted along the longitudinal direction, as shown in Figure 4(c), which is a result of the fiber drawing technique either on purpose or unintentionally[35,36], and the parameter β is defined as the square fiber twisting angle, referring to the angle difference between the square fiber output cross-section and the input cross-section, where the unit is degree (°). Then, as sketched in Figure 4(d), the square-core fiber may exhibit macro-bending of the optical axis, which is introduced by the stress remaining from fiber

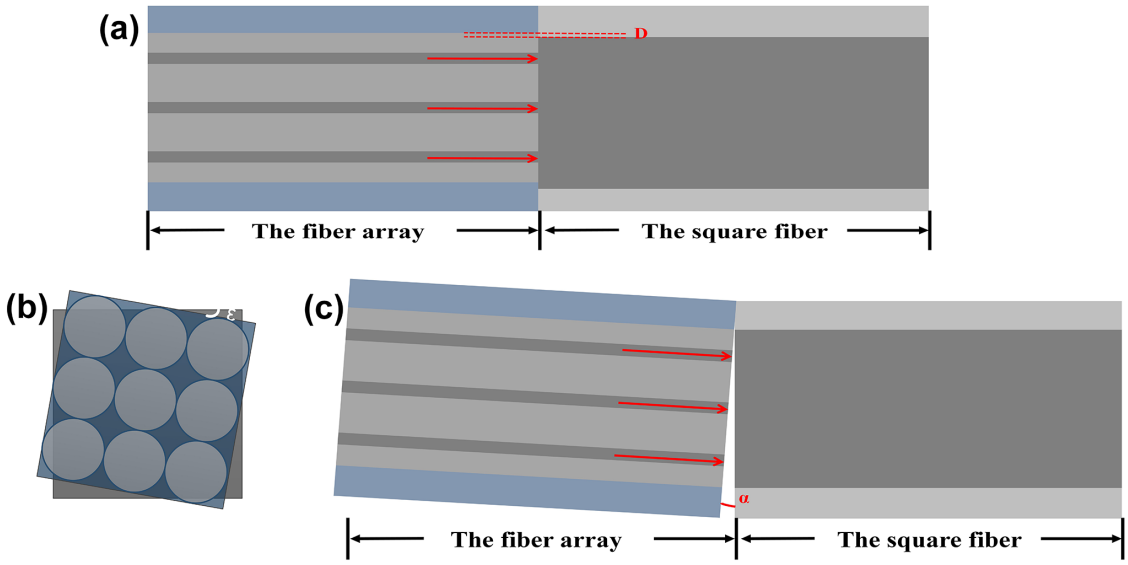

Figure 3. Diagram of (a) the transversal offset, (b) the angular offset and (c) the pointing error between the fiber array and the square-core fiber.

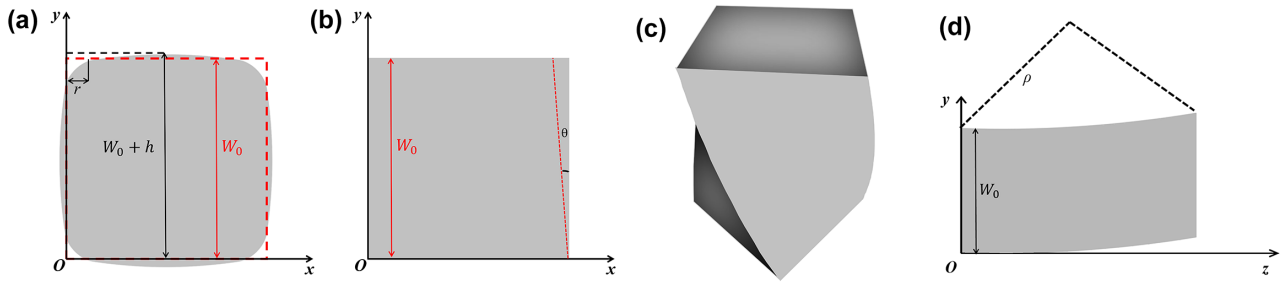

Figure 4. Diagram of (a) the core roundness, (b) the side inclination, (c) the twist and (d) the bending of square-core fiber.

coiling during storage and transportation, and the bending radius ρ is used to characterize this phenomenon.

3. Numerical simulations

Error analysis is performed by simulating the laser beam propagation along the fiber combiner and investigating the variation of the beam combining efficiency and M^2 factor, from which it is possible to provide valuable guidance to the selection of fiber material and to the fabrication of a fiber combiner for optimizing the CBC performance. The mismatch errors mentioned in the second section are all taken into account in the simulation model. To simplify the calculations, the case of a 2 × 2 combiner is taken as an example to study the influence of mismatch errors on the beam combining effect. In addition, to rule out interference between the various error factors, simulations are conducted by analyzing one factor at a time, which means that other factors are in perfect condition and do not cause mismatch issues. Both the beam quality and the combining efficiency are used to evaluate the beam combining performance: the M^2 factor is calculated by using the second-moment method over the whole beam. In this work, M^2 is calculated by fitting the beamwidth using multiple data points at different propagation distances, and the beamwidth is calculated using a second-moment definition, that is, the second moment of the intensity of the spot is defined as the beam width, which results in the value of M^2 being highly sensitive to the presence of the sidelobe, and even a small fraction of the power in the sidelobe will lead to obvious degradation of M^2. The combining efficiency is defined as the ratio of the power in the central main lobe to the total power, where the boundary of the central main lobe is determined by having the M^2 of the beam inside being around 1.1. In the presence of mismatch errors, the perfect self-imaging effects have been broken, and the ideal one spot cannot be achieved. Part of the energy, which cannot be delivered into the main lobe due to the broken self-imaging effects, formed the sidelobes, which results in the deterioration of the combination. As the mismatch error increases, more energy will be delivered into the sidelobes, so the combining efficiency was defined as the power ratio in the central lobe as previously used in Ref. [37], which contains the transmission and the power ratio in the central lobe of the intensity. The constant parameters in the simulations are as follows. The wavelength of the fiber lasers is 1.064 μm. The core diameter and numerical aperture (NA) of the 2 × 2 input fibers are 20 μm and 0.065, respectively. The core side length and NA of the square-core output fiber are 200 μm and 0.22, respectively. Besides, it is assumed that the refractive index of the core of the square-core fiber is 1.457; thus, the length of the square-core fiber is set to be 2.75 cm, which is the theoretical combining length of this 2 × 2 self-imaging combiner[29]. Based on the above assumptions, the three types of mismatch errors aforementioned are modeled and the influences on the combining performance are simulated. In the manuscript, the intensity distribution is the lateral laser intensity of the combining laser spot. The tolerance degree of different mismatched errors is also simulated when the combining efficiency decreases by 1% as the fiber array is expanded from 2 × 2 to 6 × 6, which can help one to analyze the requirements for the making process when the number of routes is expanded. In the simulation, the size of the output fiber of the fiber array is kept unchanged at 20/100 μm. When the number of channels is expanded, the size of the square fiber required will increase.

3.1. *Influences of fiber array misalignment*

The dependence of the M^2 factor and efficiency of the combined beam on the amount of position error is analyzed, as shown in Figures 5(a) and 5(b). Since all four fibers in the fiber array can have position deviations, the method of random generation of error has been used in the simulations, and more reliable results can be obtained. The simulation position error range of the fiber array is 0–3 μm. Since the position deviation of the four fibers of the fiber array is random and different, in order to establish the simulation deviation model more accurately, each group of deviations is randomly generated and calculated five times. For example, when the simulation position deviation is 1 μm, the program is used to randomly generate five groups of deviation data with an average of 1 μm and a variance of 0.05, which obey the normal distribution, and the positive and negative values

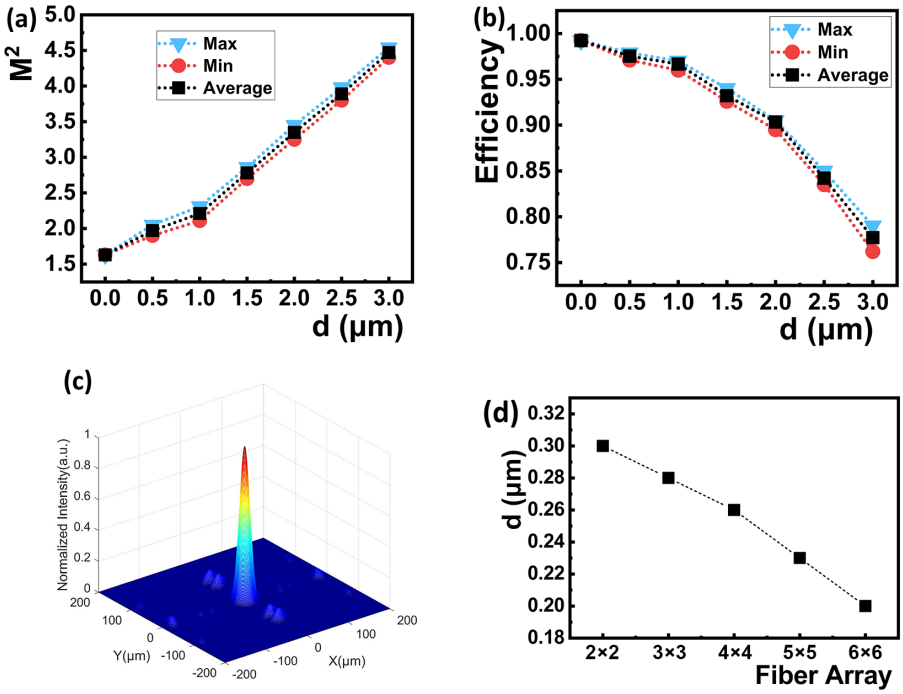

Figure 5. Dependence of (a) the beam quality and (b) the efficiency of CBC on the position error of the fiber array. (c) Intensity distribution of the combined beam influenced by position error. (d) Diagram of the tolerance to position error corresponding to 1% loss of the beam combining efficiency under different fiber arrays.

of the production data are randomly used to represent the deviation direction as (+1.10, –0.82), (–1.23, –1.19), (+1.16, +0.74), (+0.93, –0.76), (–0.81,+1.06); to further explain, position deviation (+1.10, –0.82) is the positive deviation of the *x*-axis by 1.10 μm and the negative deviation of the *y*-axis by 0.82 μm. The maximum, minimum and average combining effects under different deviation directions are given. The respective beam combination process is emulated and the overall combining performances are summarized, with the maximum, the minimum and the average statistics reported in Figures 5(a) and 5(b). It is evident that at increasing position error, the beam combining performance becomes worse. The intensity distribution of the combined beam in the case of position error, being 3 μm, is shown in Figure 5(c). Sidelobes appear around the central main lobe, which will adversely affect the beam combining efficiency and the beam quality. Because the four fibers deviate in random directions, the sidelobe appears around the main lobe. In addition, the tolerance of position deviation from the 2 × 2 fiber array expanded to a 6 × 6 fiber array with the combining efficiency loss of no more than 1% is given, as shown in Figure 5(d). This indicates that the expansion of the fiber number puts forward higher requirements for the accuracy of position deviation.

Another mismatch is the deviation of the polarization direction. By decomposing a laser into two components, one being linearly polarized along the desired direction and the other being linearly polarized along the perpendicular direction, among which only the former can participate in the coherent combination, the influence of the error of polarization direction on the beam combining performance has been simulated. The M^2 and efficiency at polarization axes differences ranging from 5° to 30° are shown in Figures 6(a) and 6(b). Similarly, the method of randomly generated error has been used and the span of M^2 and efficiency are given. The typical intensity distribution with polarization error is depicted in Figure 6(c). The sidelobes and the main lobe form a 3 × 3 arrangement, which results from the incoherent contribution of the laser light in the other polarization direction. The same as the position error, as the fiber array expands, the tolerance of the polarization error becomes more stringent in the case of 1% combining efficiency loss, which is shown in Figure 6(d).

3.2. Influences of the misalignment between the fiber array and square-core fiber

The influence of the transversal offset between the fiber array and the square-core fiber is shown in Figures 7(a) and 7(b). At an offset value changing from 0 to 3 μm, the beam combining performances are evidently deteriorated. In order to better observe the sidelobe distribution, the intensity distribution in the case of 5-μm transversal offset is shown in Figure 7(c). Sidelobes appear in the *x*-axis direction, which is because the offset is imposed along this direction. The tolerance of transversal offset is calculated in the case of 1%

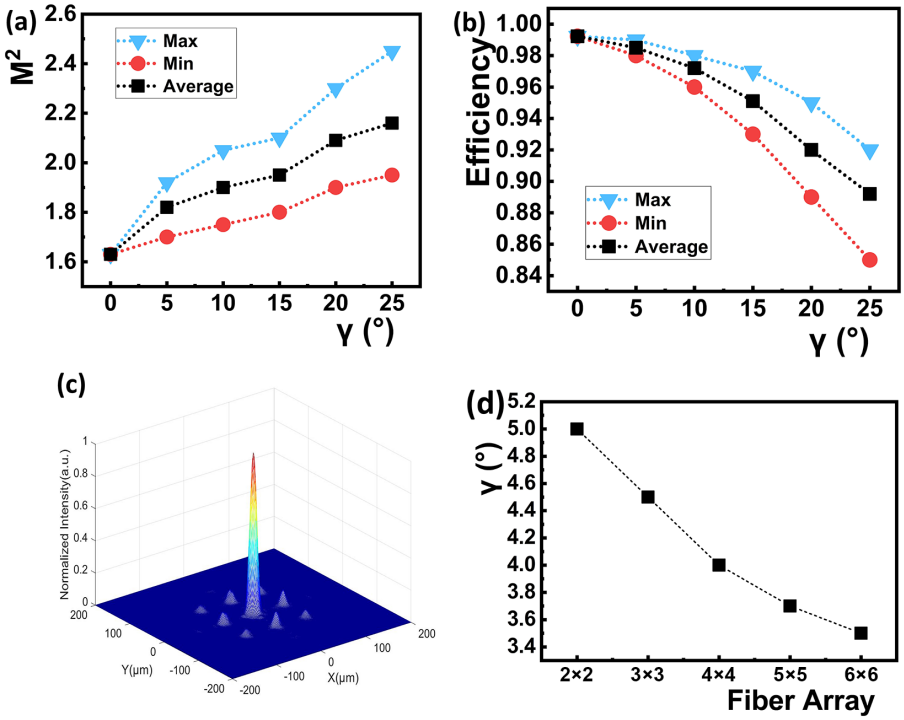

Figure 6. Dependence of (a) the beam quality and (b) the efficiency of CBC on the polarization deviation of the fiber array. (c) Intensity distribution of the combined beam influenced by polarization deviation. (d) Diagram of the tolerance to polarization direction error corresponding to 1% loss of beam combining efficiency under different fiber arrays.

combining efficiency loss as the fiber array expands, which is shown in Figure 7(d). In special cases, the transversal offset can be equivalent to the position error of the fiber array, so with the increase of the array, the tolerance has the same tendency to become stricter.

The influence of angular offset between the fiber array and the square-core fiber on the beam combining performance is shown in Figures 8(a) and 8(b). Obviously, the performance becomes worse with the increase of the angular offset. The typical intensity distribution resulting from angular offset is shown in Figure 8(c). The sidelobes are mainly distributed in the four corners of the square core of the output fiber, and the overall shape exhibits a rotation with respect to the geometry of the square core. The tolerance of the angular offset when the combining efficiency decreases 1% is calculated in Figure 8(d). With the increase of the number of fibers, higher requirements are put forward for angular offset.

The results of the combining performance influenced by the pointing error are shown in Figures 9(a) and 9(b). With a similar trend, the pointing error adversely affects the combining performance, and when the pointing error is larger than 0.4°, the performance starts deteriorating significantly. The intensity distribution resulting from the pointing error shown in Figure 9(c) implies that the sidelobes appear in the same direction as the pointing error, which is similar to the phenomenon induced by transversal offset. The tolerance of the pointing error is calculated in the case of 1% combining efficiency loss as the fiber array expands, which is shown in Figure 9(d). Different from the above deviation, the tolerance of the pointing error becomes more relaxed with the increase of the fiber array. However, the range of tolerance changes is so small that it can be ignored.

3.3. *Influences of the square-core fiber geometry*

The influence of the roundness of square-core corners on the combining performance is shown in Figures 10(a) and 10(b). It can be seen from the results that small rounded corners, for example, with the radius of curvature being less than 10 μm, have a minor effect on the beam combining quality and efficiency. However, when the roundness continues to increase, the combining performance is adversely affected at a sharp rate. A typical intensity distribution with the impact of corners rounding is shown in Figure 10(c). Sidelobes closely connected to the main lobe are generated. When the combining efficiency decreases by 1%, the tolerance curve of the rounded corner of the square fiber with the increase of the fiber array is given, as shown in Figure 10(d). As the array increases, the tolerance of the radius of rounded corners becomes more relaxed, which is also related to the reason that the size of square fiber required increases with the increase of the array.

The straightness of the four square sides has a strong impact on the beam combining performance, as Figures 11(a) and 11(b) show, which is because curved edge borders

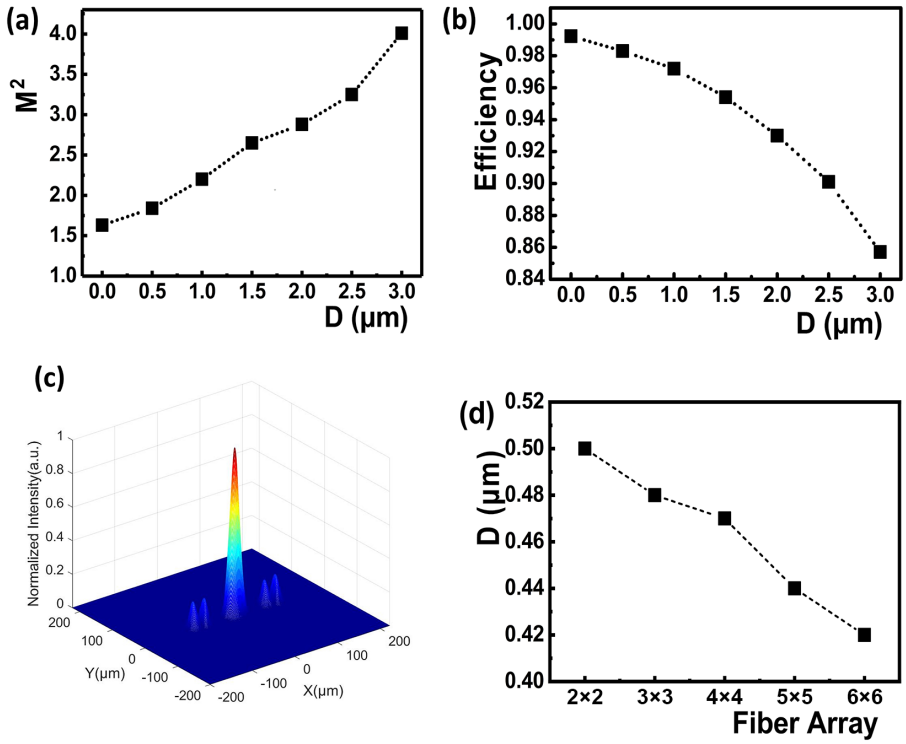

Figure 7. Dependence of (a) the beam quality and (b) the efficiency of CBC on the transversal offset between the fiber array and the square-core fiber. (c) Intensity distribution of the combined beam influenced by transversal offset. (d) Diagram of the tolerance to transversal offset corresponding to 1% loss of beam combining efficiency under different fiber arrays.

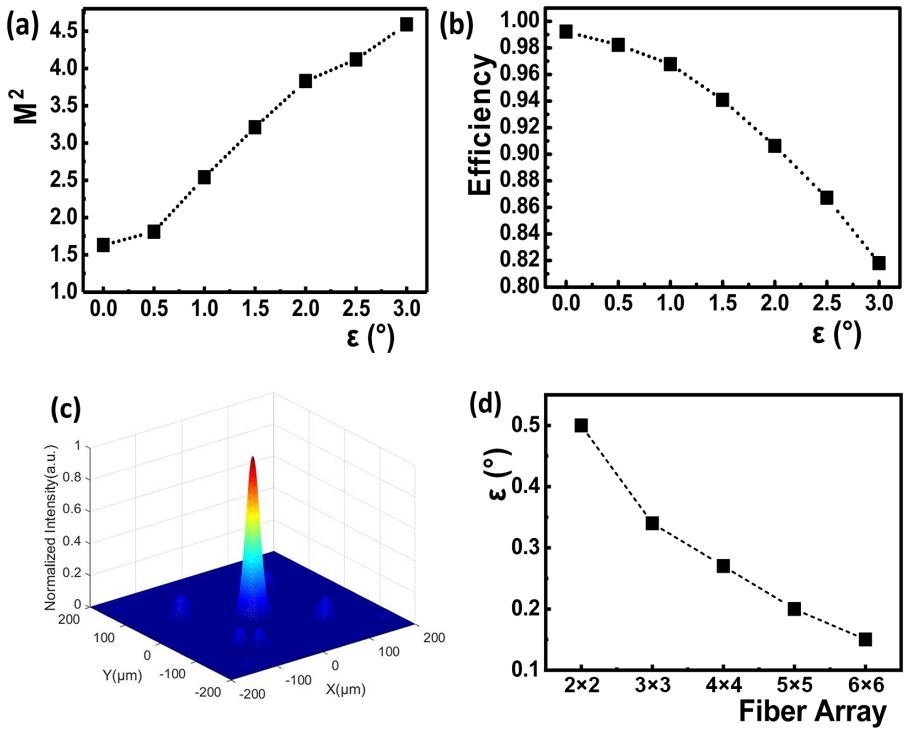

Figure 8. Dependence of (a) the beam quality and (b) the efficiency of CBC on the angular offset between the fiber array and the square-core fiber. (c) Intensity distribution of the combined beam influenced by angular offset. (d) Diagram of the tolerance to angular offset corresponding to 1% loss of beam combining efficiency under different fiber arrays.

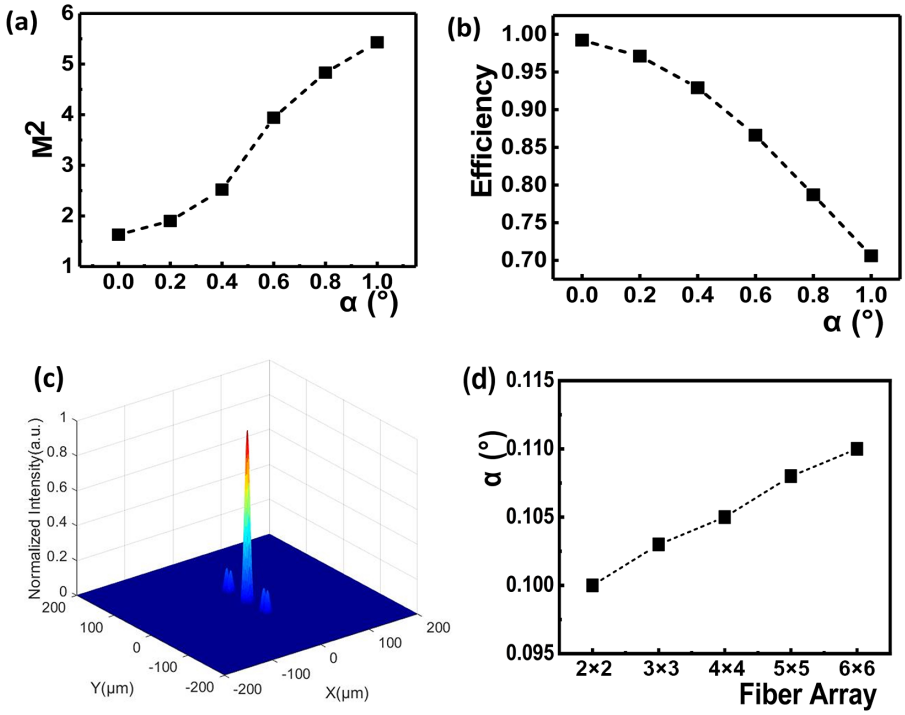

Figure 9. Dependence of (a) the beam quality and (b) the efficiency of CBC on the pointing error between the fiber array and the square-core fiber. (c) Intensity distribution of the combined beam influenced by the pointing error. (d) Diagram of the tolerance to pointing error corresponding to 1% loss of beam combining efficiency under different fiber arrays.

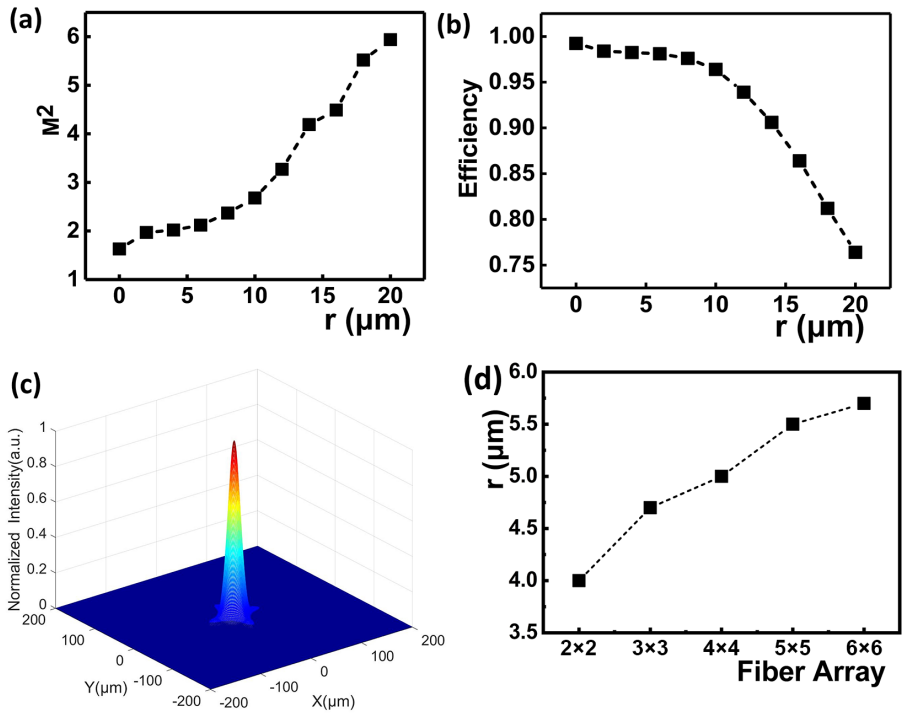

Figure 10. Dependence of (a) the beam quality and (b) the efficiency of CBC on the corner radius of the square-core fiber. (c) Intensity distribution of the combined beam influenced by rounded corners. (d) Diagram of the tolerance to rounded corners corresponding to 1% loss of beam combining efficiency under different fiber arrays.

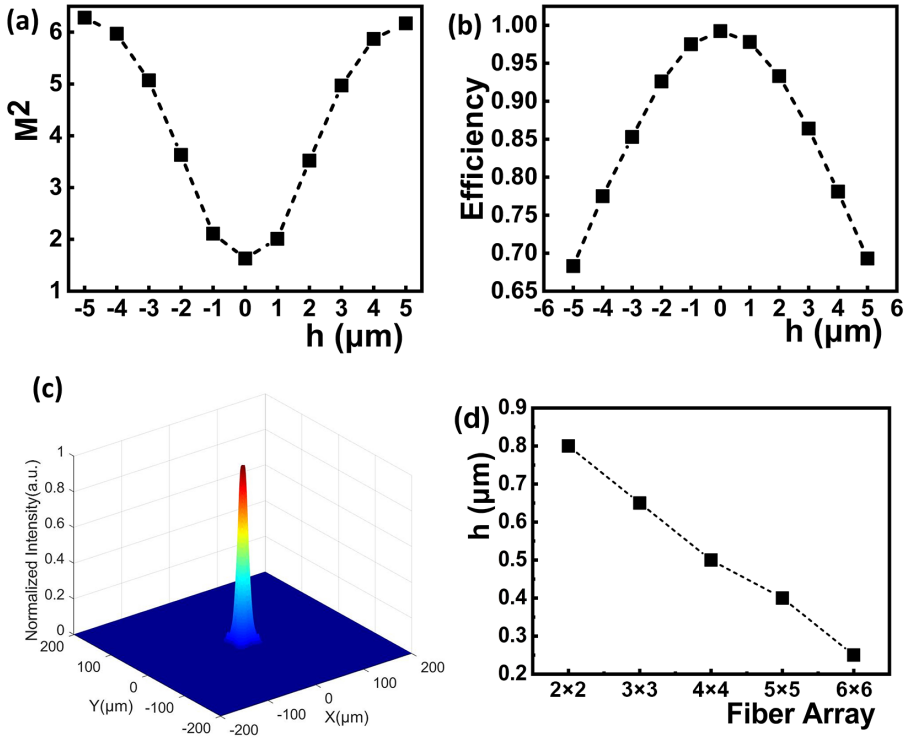

Figure 11. Dependence of (a) the beam quality and (b) the efficiency of CBC on the side straightness of the square-core fiber. (c) Intensity distribution of the combined beam influenced by curved edge borders. (d) Diagram of the tolerance to curved edge borders corresponding to 1% loss of beam combining efficiency under different fiber arrays.

of the square-core fiber will directly impair the self-imaging process of the laser beams. Here the positive and negative values of the deviation symbol h represent the convex and concave edge borders, respectively. It is shown that concave edges appear to deteriorate the beam combining performance a little more than the convex cases. The intensity distribution in Figure 11(c) implies that sidelobes are close to the main lobe, and the energy is transferred to the sidelobe. The distribution of the sidelobe is not neat and uniform, and is more chaotic. In addition, the tolerance of curved edge borders from the 2 × 2 fiber array expanded to a 6 × 6 fiber array with the combining efficiency loss of no more than 1% is given, as shown in Figure 11(d). With the increase of the array, the tolerance of curved edge borders has an obvious downward trend, indicating that the influence of the round edge on the combining effect becomes greater with the increase of the array.

The influence of the slanted edge of the square core is shown in Figures 12(a) and 12(b). The intensity distribution when θ equals 3° is shown in Figure 12(c). The sidelobes of the combined beam are also distributed around the main lobe, but are significantly larger and more irregular. Considerable power transfer from the main lobe to the sidelobes indicates that the combining performance is impacted greatly by the core side inclination, which should be treated stringently. When the combining efficiency decreases by 1%, the tolerance curve of the slanted edge of the square core with the increase of the fiber array is given, as shown in Figure 12(d). This further shows that the slanted edge has a great influence on the beam combining efficiency, and with the increase of the array, the requirement of the slanted edge becomes more stringent.

The twist of the square-core fiber along the longitudinal direction obviously deteriorates the beam combining performance, which is shown in Figures 13(a) and 13(b). As illustrated in Figure 13(c), the combined beam with the influence of square-core fiber twisting exhibits sidelobes distributed at the four corners and sidelobes next to the main lobe, and the angle of twist can be reflected from the contour of the peripheral sidelobes. In the 2 × 2 array beam combining, when the beam combining efficiency is 1% loss, a twist angle of 1.5° can be tolerated. When the 2 × 2 fiber array is expanded to a 6 × 6 fiber array, the tolerance to twist is reduced to 0.5°, as shown in Figure 13(d), when the beam combining efficiency is still maintained at a 1% loss. As the fiber array increases, the tolerance to twist becomes more stringent.

The influence of the bending of the square-core fiber is shown in Figures 14(a) and 14(b). The horizontal axis is the bending radius, which is inversely proportional to the amount of fiber bending and, thus, the smaller the bending on the fiber, the better the coherent beam combining performance. The intensity distribution of the combined beam that results from fiber bending with radius ρ being 20 m

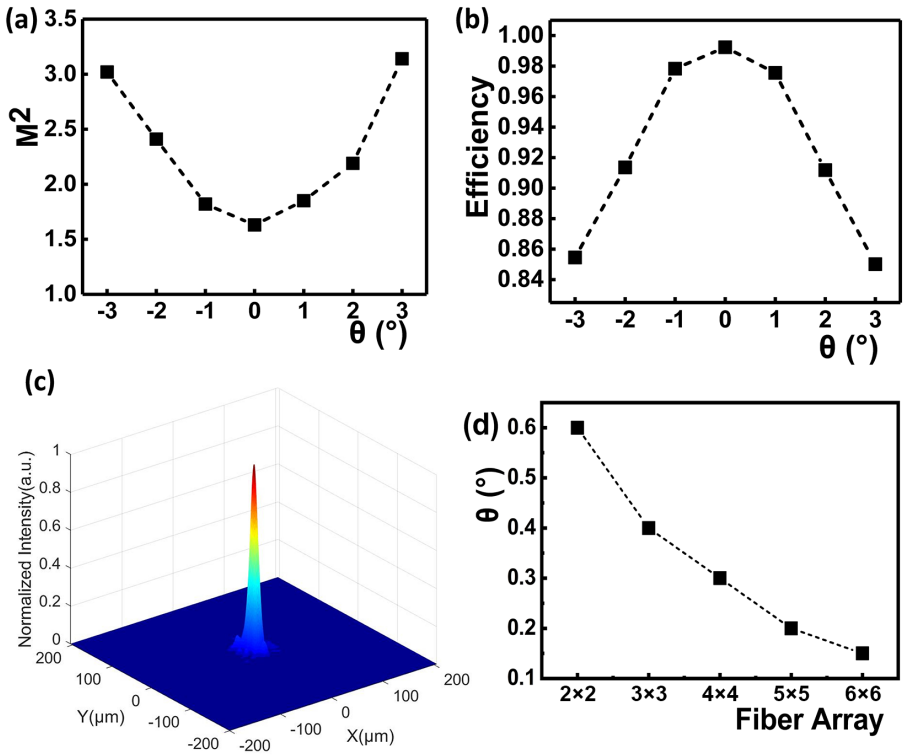

Figure 12. Dependence of (a) the beam quality and (b) the efficiency of CBC on the side inclination of the square-core fiber. (c) Intensity distribution of the combined beam influenced by slanted edge borders. (d) Diagram of the tolerance to slanted edge borders corresponding to 1% loss of beam combining efficiency under different fiber arrays.

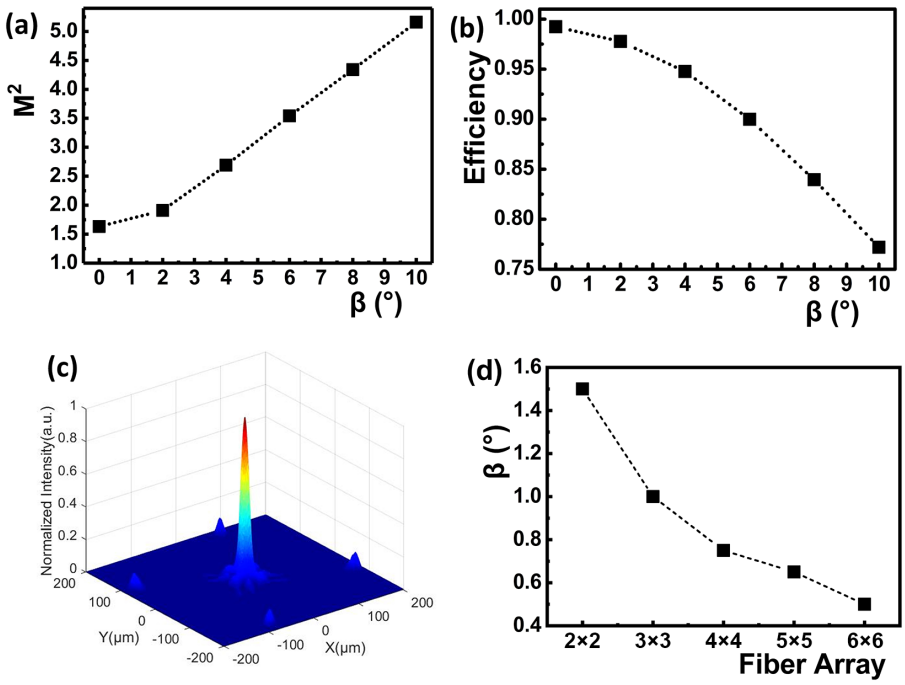

Figure 13. Dependence of (a) the beam quality and (b) the efficiency of CBC on the twist angle of the square-core fiber. (c) Intensity distribution of the combined beam influenced by the square-core fiber twist. (d) Diagram of the tolerance to square-core fiber twist corresponding to 1% loss of beam combining efficiency under different fiber arrays.

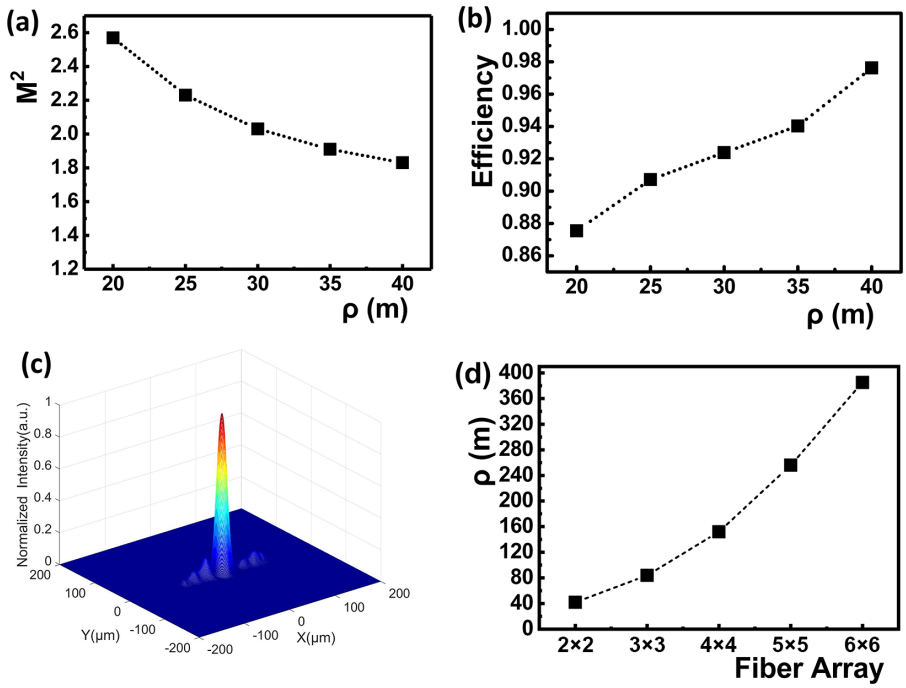

Figure 14. Dependence of (a) the beam quality and (b) the efficiency of CBC on the bending radius of the square-core fiber. (c) Intensity distribution of the combined beam influenced by square-core fiber bending. (d) Diagram of the tolerance to square-core fiber bending corresponding to 1% loss of beam combining efficiency under different fiber arrays.

is shown in Figure 14(c). The sidelobes appear along the same direction as the fiber bending direction. The sidelobes are asymmetrically distributed on the two sides of the main lobe, and are distributed along the curved direction. Since the bending degree of the two sides of the square-core fiber after bending is different, one is bent inward and the other is bent outward, so the size and distribution of the sidelobes are also different. In the 2 × 2 array beam combining, when the beam combining efficiency decreases by 1%, the bending radius of 42 m can be tolerated. When the 2 × 2 fiber array is expanded to a 6 × 6 fiber array, a larger bending radius is required, that is, the requirements for the bending radius are stricter.

4. Discussion

Based on the theoretical investigations in Section 3, it is concluded that all the mismatch errors can adversely affect the coherent beam combining performance, but to varying degrees, and different types of mismatch error can induce different patterns of sidelobes, which is useful for searching for the dominant deviations according to the shape of the combined spot during experiments. In order to provide references for the fabrication of self-imaging combiners and for the development of all-fiber CBC, tolerance analyses have also been performed, in which the combining efficiency being 1% loss has been used as the inclusion criterion, and the allowed limit of each mismatch error is as reported in Table 1.

As shown, the 10 kinds of mismatches, which separately induce 1% of loss, would generate a combined loss of about 10% if all impact simultaneously. This means that for a 2 × 2 self-imaging combiner to achieve 90% combination efficiency, the position error, polarization deviation, transversal offset, angular offset, pointing error, corner radius, side straightness, side inclination, twist angle and bending radius should be controlled within 0.3 μm, 5°, 0.5 μm, 0.5°, 0.1°, 4 μm, 0.8 μm, 0.6°, 1.5° and 42 m, respectively. Apart from the simplest 2 × 2 combination case, self-imaging combiners with the combination channels expanding to 6 × 6 have also been simulated and the corresponding tolerances are compared in Table 1. In the simulations, it is assumed that the size of the input fiber is maintained while the size of the square-core output fiber varies with the fiber array configuration. According to the listed results in Table 1, the variation tendencies of the tolerances are revealed. With the increasing of combination channels, almost all the mismatch errors show much stricter requirements, except for the pointing error and the corner radius. Therefore, more stringent control on the mismatches should be taken into account in scaling the channel number of all-fiber self-imaging CBC.

The theoretical simulation discussed above only considered fundamental modes and did not account for higher-order modes in the input fiber laser. However, higher-order modes are inevitably present in practical use. To investigate their impact on the simulation results of a square fiber combiner, simulation studies and discussions were conducted. Taking a 2 × 2 fiber array as an example, the proportions of

Table 1. Tolerance for mismatch errors at 1% combining efficiency loss.

Type of mismatch error		Error tolerance at 1% combining efficiency loss					Variation of tolerance with the increasing combination channels
		2 × 2	3 × 3	4 × 4	5 × 5	6 × 6	
Alignment error of fiber array	Position error (μm)	0.30	0.28	0.26	0.23	0.20	Stricter
	Polarization deviation (°)	5.0	4.5	4.3	3.7	3.5	Stricter
Assembly error between fiber array and square-core fiber	Transversal offset (μm)	0.50	0.48	0.47	0.44	0.42	Stricter
	Angular offset (°)	0.5	0.34	0.27	0.2	0.15	Stricter
	Pointing error (°)	0.100	0.103	0.105	0.108	0.110	Barely changed
Geometric error of square-core fiber	Corner radius (μm)	4.0	4.7	5.0	5.5	5.7	More relaxed
	Side straightness (μm)	0.80	0.65	0.50	0.40	0.25	Stricter
	Side inclination (°)	0.60	0.40	0.30	0.20	0.15	Stricter
	Twist angle (°)	1.50	1.00	0.75	0.65	0.50	Stricter
	Bending radius (m)	42	84	152	256	385	Stricter

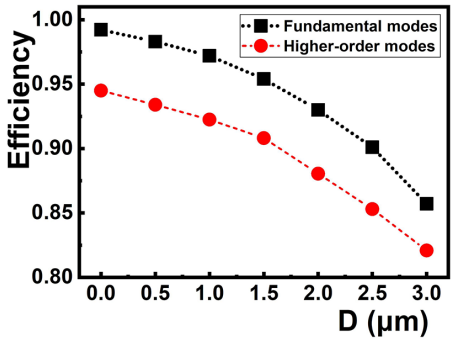

Figure 15. The combining efficiency of the fundamental mode and the high-order mode varies with different welding position deviations.

fibers with higher-order modes in the four fibers were set to 5%, 10%, 15% and 20%, respectively. Since most higher-order modes are LP11 mode[38–40], only the influence on coupling efficiency was simulated. Due to the random and uncontrollable polarization of higher-order mode lasers, the higher-order modes in the four fibers were set to be different and randomly distributed in the simulation. The influence of the deviation of the fusion position between the fiber array and the square fiber on the combining efficiency was simulated in the case of the existence of a higher-order mode laser, and the results are shown in Figure 15. The black solid line in Figure 15 represents the combining efficiency when the input fiber laser consists solely of fundamental modes. The red circle curve represents the combining efficiency when higher-order modes are present in the input laser. The simulation results indicate that the presence of higher-order modes does impact the combining efficiency. However, as the fusion position deviation increases, the trend is similar to that of the fundamental mode case. Similarly, the simulation result can be extrapolated to other deviation scenarios, suggesting that higher-order modes do affect the combining efficiency, but they do not significantly alter the trend of changes in combining efficiency under deviation.

Besides higher-order modes, the thermal effect is also one of the important factors affecting the combining effect. The thermal effect will bring changes in the size and refractive index of the square fiber. In Ref. [29], we calculated and analyzed the shape variables of square fiber caused by a temperature increase; the results showed that the shape variables caused by a temperature increase were very small and the influence on the combining results of square fiber combiners could be negligible. The refractive index is a function of wavelength, temperature and stress[41]. As the output power of a laser gradually increases, the quantum loss effect generates thermal effects, leading to changes in the refractive index and stress of the fiber due to thermal diffusion in the material. In the case of square fibers, which are typically of centimeter scale for a coherent combination, and since the square fiber serves as the output end without being subjected to stress constraints, the influence of the temperature increase on stress can be neglected. Therefore, this discussion focuses on the impact of the temperature increase on the refractive index of square fibers and the subsequent effect on beam combining. The refractive index of the fiber can be expressed using the following formula[41]:

$$n(\lambda, T, X) = n(\lambda, T_0) + C_1(T - T_0) + C_2 X, \quad (1)$$

where $n(\lambda, T_0)$ is the refractive index at a fixed wavelength, fixed initial temperature and zero stress. For the square fiber in coherent synthesis, the refractive index of the square fiber at 1064 nm, 20°C room temperature and zero stress state is 1.45. Here, T is the rising temperature, X is the stress state, which is considered to be 0, and C_1 and C_2 are temperature coefficients and stress coefficients, respectively, where for quartz fiber, $C_1 = 1.18 \times 10^{-5}$[42]. The transmission process of laser spots in square fiber is generally distributed by multiple images, and the combination of lasers is only realized in the last short length. Therefore, in the process of spot transmission, the energy distribution is relatively uniform, the temperature increase is not obvious and the

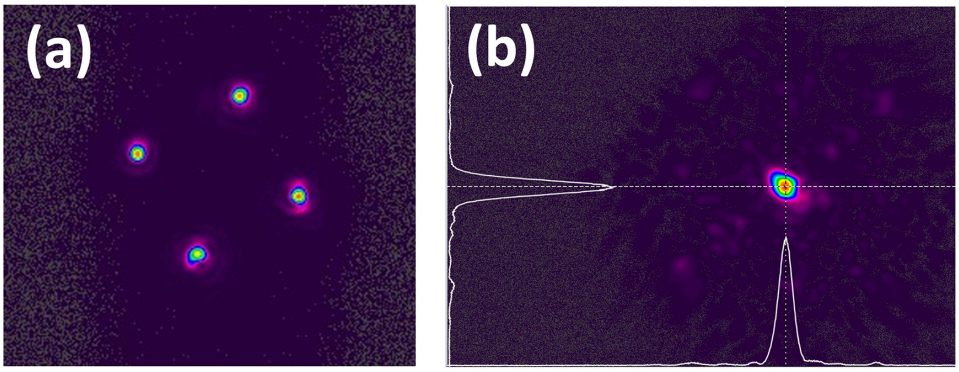

Figure 16. (a) Diagram of the spot array output by the fiber array. (b) Diagram of the combining spot.

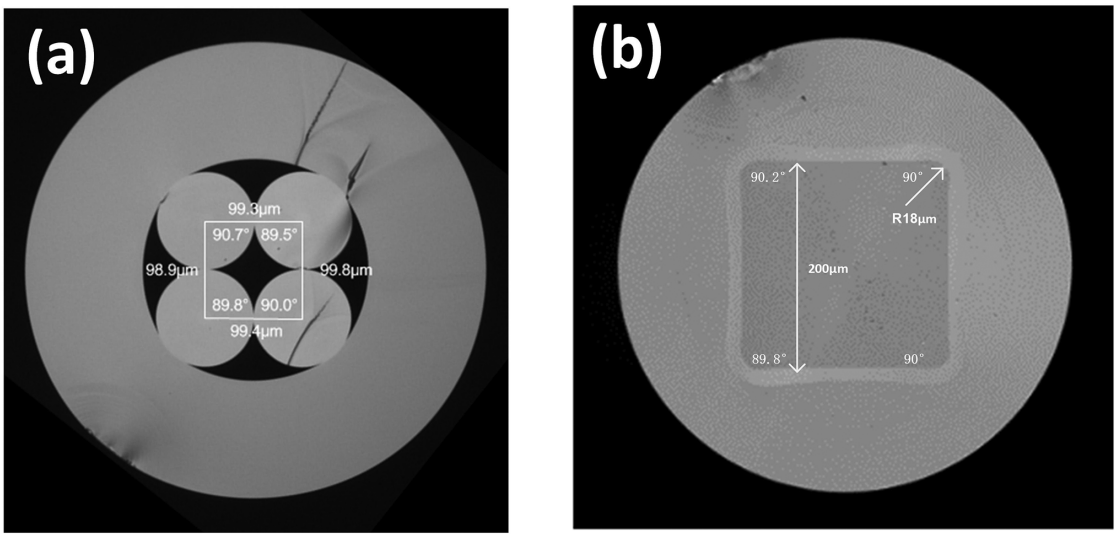

Figure 17. Microscopic images of the 2 × 2 self-imaging combiner: (a) on the fiber array side; (b) on the square-core fiber side.

change of refractive index can be ignored. When the lasers are combined into a spot in the last small length of the square fiber, the energy is more concentrated and the temperature increases significantly. When the center temperature of the square fiber is increased to 100°C, the central refractive index of the square fiber changes from 1.45 to 1.4509 and simulation shows that it has negligible effect on the combining effect. The above calculation results show that when the temperature of the square fiber is increased to 100°C, the thermal effect has little influence on the combining effect, and a further substantial increase in temperature may have a greater impact on the combining effect. Besides, there are also very mature cooling methods, such as water cooling after packaging, to dissipate the waste heat in optical fiber components.

In order to verify the theoretical modeling and simulation results of all-fiber self-imaging CBC, a 2 × 2 combiner has been made and preliminary CBC tests have been carried out[31]. Passive fiber with a 20-μm diameter and NA = 0.065 core was used as the input, and square-core fiber with the core side length being 200 μm and NA being 0.22 was adopted as the output of the self-imaging combiner, for which the cross-sectional microscopic images on the input and output sides are depicted in Figure 16. Figure 16(a) is the 2 × 2 spot array output by the fiber array, and Figure 16(b) is the combining spot. The beam combining efficiency was measured to be 52.7%.

The cross-sectional microscopic images on the input and output sides are depicted in Figure 17. As can be seen from Figure 17(a), the position errors of the four fibers in the fiber array are 0.7, 0.2, 1.1 and 0.6 μm, respectively, corresponding to theoretical loss of about 3%. Since the beam combiner is a non-polarization-maintained device, four manual polarization control devices are added to the front beam combiner system. After measurement, the error of manual polarization control is about 5°, and 2% of the combiner efficiency is lost according to the simulation results. The glass tube of the fiber array is 1.8 μm eccentric, resulting in a 1.8 μm weld position error and a 6% loss of combining efficiency. The cutting angle of the fiber array and square fiber is kept below 0.2°, resulting in a pointing deviation of about 0.2°. At the same time, the fiber array and square fiber are carefully

manually aligned to realize the matching of the cross-section shape in the fusion process, with only a welding distortion deviation of about 0.5°, which reduces the beam combining efficiency by 3% and 1%, respectively.

From Figure 17(b), the cross-section of the square fiber has round corners of 18 μm. According to the theoretical simulation results, 19% of the combining efficiency is lost. The four sides of the square fiber core have an inner concave of about 2 μm, which results in a loss of 6% of the combining efficiency. One side of the square fiber has a bevel angle of 0.2°, and the loss of combining efficiency is about 1%. The square fiber is fixed in the experiment, so the effect of the bending of the square-core fiber combination is ignored.

After the analysis of the errors, the total loss of the beam combining efficiency is about 41% and, in addition, the beam quality of the output of the fiber laser used in combination is M^2 ~ 1.2, which is not perfect single-mode output, and the control accuracy and bandwidth of the phase control will also have a certain impact on the combining efficiency. It shows that the theoretical model of the beam combining device deviation and the simulation of the effect of the mismatch error on the beam combining effect are very consistent with the experimental results, further illustrating the reliability and guiding significance of the theoretical simulation results. It can be seen from the theoretical calculation results that the error of the square-core fiber is the main factor affecting the combining efficiency at present, among which the rounded corners of the square cross-section have a greater influence. In the following research, while reducing the mismatch errors of the square fiber and fusion, emphasis should be placed on using the square-core fiber with a perfect section and small distortion to improve the combining efficiency.

5. Conclusion

In this paper, the mismatch errors of the beam combiner are investigated numerically. According to the structure of the beam combiner, the errors have been divided into three categories, which were numerically studied by the FDBPM. It is shown that the mismatch errors affect the self-imaging effect in the square fiber, and then affect the combining performance. With different mismatch errors, the sidelobe of the combining beam spot has different distributions. The tolerance of each mismatch error is calculated with 1% efficiency loss being the criterion, and the trend is summarized. It is revealed that with the expansion of the number of channels, the tolerances of the pointing error in the welding process and the rounded corners of the square fiber become more relaxed, and other tolerances of deviation become stricter. Finally, the theoretical model results are used to analyze the experimental results, and the theoretical simulation results are in good agreement with the experimental results, which proves the reliability of the theoretical model and the simulation results. This work can provide guidance for the design and fabrication of an all-fiber combining device based on the self-imaging effect.

References

1. M. N. Zervas and C. A. Codemard, IEEE J. Sel. Top. Quantum Electron. **20**, 23 (2014).
2. Z. Liu, X. Jin, R. Su, P. Ma, and P. Zhou, Sci. China-Inf. Sci. **62**, 041301 (2019).
3. W. Shi, Q. Fang, X. Zhu, R. A. Norwood, and N. Peyghambarian, Appl. Opt. **53**, 6554 (2014).
4. S. Fu, W. Shi, Y. Feng, L. Zhang, Z. Yang, S. Xu, X. Zhu, R. A. Norwood, and N. Peyghambarian, J. Opt. Soc. Am. B **34**, A49 (2017).
5. P. Zhou, H. Xiao, J. Leng, J. Xu, Z. Chen, H. Zhang, and Z. Liu, J. Opt. Soc. Am. B **34**, A29 (2017).
6. G. Mourou, B. Brocklesby, T. Tajima, and J. Limpert, Nat. Photonics **7**, 258 (2013).
7. J. J. Zhu, P. Zhou, Y. X. Ma, X. J. Xu, and Z. J. Liu, Opt. Express **19**, 18645 (2011).
8. R. M. Tao, X. L. Wang, and P. Zhou, IEEE J. Sel. Top. Quantum Electron. **24**, 0903319 (2018).
9. M. N. Zervas, Opt. Express **27**, 19019 (2019).
10. C. Jauregui, J. Limpert, and A. Tünnermann, Nat. Photonics **7**, 861 (2013).
11. B. Shiner, in *CLEO: 2013*, OSA Technical Digest (online) (Optica Publishing Group, 2013), paper AF2J.1.
12. S. J. Augst, J. K. Ranka, T. Y. Fan, and A. Sanchez, J. Opt. Soc. Am. B **24**, 1707 (2007).
13. A. Flores, I. Dajani, R. Holten, T. Ehrenreich, and B. Andersona, Opt. Eng. **55**, 096101 (2016).
14. Z. J. Liu, P. F. Ma, R. T. Su, R. M. Tao, Y. X. Ma, X. L. Wang, and P. Zhou, J. Opt. Soc. Am. B **34**, A7 (2017).
15. E. Shekel, Y. Vidne, and B. Urbach, Proc. SPIE **11260**, 1126021 (2020).
16. M. Muller, C. Aleshire, A. Klenke, E. Haddad, F. Legare, A. Tunnermann, and J. Limpert, Opt. Lett. **45**, 3083 (2020).
17. P. F. Ma, H. X. Chang, Y. X. Ma, R. T. Su, Y. F. Qi, J. Wu, C. Li, J. H. Long, W. C. Lai, Q. Chang, T. Y. Hou, P. Zhou, and J. Zhou, Opt. Laser Technol. **140**, 5 (2021).
18. G. D. Goodno and S. B. Weiss, Opt. Express **20**, 14945 (2012).
19. C. Geng, W. Luo, Y. Tan, H. M. Liu, J. B. Mu, and X. Y. Li, Opt. Express **21**, 25045 (2013).
20. L. A. Beresnev, T. Weyrauch, M. A. Vorontsov, L. Liu, and G. W. Carhart, Proc. SPIE **7090**, 709008 (2008).
21. D. Zhi, Y. X. Ma, Z. L. Chen, X. L. Wang, P. Zhou, and L. Si, Opt. Lett. **41**, 2217 (2016).
22. Y. Shamir, R. Zuitlin, Y. Glick, M. Aviel, N. Shafir, R. Feldman, A. Dahan, B. Urbach, D. Levy, E. Shekel, and Y. Sintov, Proc. SPIE **8963**, 89630H (2014).
23. C. M. Lei, Z. X. Li, H. Zhang, Z. L. Chen, and J. Hou, Opt. Laser Technol. **130**, 106353 (2020).
24. X. Chen, T. Yao, L. Huang, Y. An, H. Wu, Z. Pan, and P. Zhou, Adv. Fiber Mater. **5**, 59 (2022).
25. V. A. Kozlov, J. Hernandez-Cordero, and T. F. Morse, Opt. Lett. **24**, 1814 (1999).
26. B. S. Wang, E. Mies, M. Minden, and A. Sanchez, Opt. Lett. **34**, 863 (2009).
27. A. A. Fotiadi, O. L. Antipov, and P. Megret, Front. Guided Wave Opt. Optoelectron. **20**, 209 (2010).
28. J. Montoya, C. Aleshire, C. Hwang, N. K. Fontaine, A. Velazquez-Benitez, D. H. Martz, T. Y. Fan, and D. Ripin, Opt. Express **24**, 3405 (2016).

29. Y. Yan, Y. Liu, H. Zhang, Y. Li, Y. Li, X. Feng, D. Yan, J. Wang, H. Lin, F. Jing, W. Huang, and R. Tao, Photon. Res. **10**, 444 (2022).
30. Y. Liu, Y. Li, Y. Li, Z. Huang, Y. Yan, X. Feng, M. Li, W. Wu, S. Huang, R. Tao, H. Lin, J. Wang, and F. Jing, in *Laser Congress 2021 (ASSL, LAC)* (Optica Publishing Group, 2021), paper JTu1A.19.
31. Y. Liu, Y. Li, Y. Yan, Y. Li, S. Huang, W. Wu, H. Lin, J. Wang, and R. Tao, Opt. Lett. **48**, 1538 (2023).
32. R. Scarmozzino and R. M. Osgood, J. Opt. Soc. Am. A **8**, 724 (1991).
33. R. Scarmozzino, A. Gopinath, R. Pregla, and S. Helfert, IEEE J. Sel. Top. Quantum Electron. **6**, 150 (2000).
34. M. Bachmann, P. A. Besse, and H. Melchior, Appl. Opt. **33**, 3905 (1994).
35. O. Blomster and M. Blomqvist, in *Proceedings of the Fourth International WLT Conference on Lasers* (2007), p. 5.
36. M. Blomqvist, S. Campbell, J. Latokartano, and J. Tuominen, Proc. SPIE **8239**, 82390L (2014).
37. R. Uberna, A. Bratcher, T. G. Alley, A. D. Sanchez, A. S. Flores, and B. Pulford, Opt. Express **18**, 13547 (2010).
38. S. Wielandy, Opt. Express **15**, 15402 (2007).
39. L. Huang, L. Kong, J. Leng, P. Zhou, S. Guo, and X. A. Cheng, J. Opt. Soc. Am. B **33**, 1030 (2016).
40. R. Tao, L. Huang, M. Li, B. Shen, X. Feng, L. Xie, J. Weng, and D. Zhi, Front. Physics **11**, 1082086 (2023).
41. L. B. Yuan, Acta Opt. Sin. **17**, 114 (1997).
42. J. W. Dawson, M. J. Messerly, R. J. Beach, M. Y. Shverdin, E. A. Stappaerts, A. K. Sridharan, P. H. Pax, J. E. Heebner, C. W. Siders, and C. P. J. Barty, Opt. Express **16**, 13240 (2008).